5D.3 TROPICAL CYCLONE-RADIATION INTERACTION IN NASA REANALYSIS AND MODEL PRODUCTS AS COMPARED TO CLOUDSAT OBSERVATIONS

Tsung-Yung Lee* and Allison A. Wing
Florida State University, Tallahassee, Florida

1. INTRODUCTION

Climate models have been utilized for understanding the relationship between tropical cyclone (TC) properties, large-scale environment, climate variability and climate change (Camargo and Wing 2016). However, the representation of TCs in climate models and reanalyses which involve data assimilation in the numerical weather prediction models (Parker 2016) are subject to errors and biases in TC properties such as TC intensity, precipitation and structure (Wing et al. 2019; Jones et al. 2021; Dirkes et al. 2023). Radiative feedbacks have been considered as one of the factors that contribute to convective organization and TC development (e.g. Wing and Emanuel 2014; Wing et al. 2016; Ruppert et al. 2020; Carstens and Wing 2020, 2022a, b; Lee and Wing 2024). The cloud-infrared radiation feedback warms the mid-troposphere in the inner core of TCs relative to clear-sky cooling in the environment. This radial gradient of warming from infrared radiation can induce a transverse circulation and support the moistening in the inner core, favoring TC development. It is of great importance to investigate the representation of the TC-radiative interactions in climate models, reanalyses and observational measurements. Specifically, the dependence of TC-radiative interactions on TC intensity will be performed. The TC-radiative interactions in the National Aeronautics and Space Administration (NASA) reanalysis and model Products will be examined and compared to that from the CloudSat tropical cyclone overpasses dataset.

2. METHODOLOGY

The CloudSat TC (CSTC) overpass dataset (Tourville et al. 2015) is used to investigate the cloud-radiative feedback from an observational perspective. The time span of the CSTC dataset ranges from 2006 to 2019. With the cloud properties measured by CloudSat (Austin et al. 2009; Deng et al. 2010, 2013, 2015; Austin and Wood 2018) and the collocated water vapor data from the European Centre for Medium-Range Weather Forecast (ECMWF; Uppala et al. 2005), the radiative fluxes and heating is evaluated by utilizing the Rapid Radiative Transfer Model for General circulation models (RRTMG; Mlawer et al., 1997; Clough et al., 2005; Iacono et al., 2008). The horizontal grid spacing is 1.7 (along-track) ×1.4 (cross-track) km^2 with 240-m vertical resolution.

Composites in radius-height diagrams for all overpasses are conducted to demonstrate general features of thermodynamic, cloud and radiative structure in TCs with a radial spacing of 3 km. The composites are categorized by TC intensity (binned by 3 m s^{-1}) of each overpass which is obtained from the International Best Track Archive for Climate Stewardship (IBTrACS; Knapp et al. 2010, 2018; Kruk et al. 2010) database. In addition, only the overpasses prior to each TC reaching its lifetime maximum intensity for the first time are included. The intensification rate composite includes 765 TC cases, 2,931 overpasses and 4,181,624 satellite footprints in total.

The Modern-Era Retrospective Analysis for Research and Application, version 2 (MERRA-2; Gelaro et al., 2017) reanalysis and one ensemble member of the MERRA-2 Atmospheric Model Intercomparison Project (AMIP) set of simulations (M2AMIP) from the National Aeronautics and Space Administration (NASA) will be examined. Both utilized the Goddard Earth Observing System (GEOS) atmospheric model (Rienecker et al., 2008; Molod et al., 2015) and analysis system (Wu et al., 2002; Kleist et al., 2009), version 5.12.4. The major difference between MERRA2 and M2AMIP is the data assimilation process applied in generating MERRA2 (Aarons et al. 2021). The grid spacing is 0.5° ×0.625° for both MERRA2 and M2AMIP with 72 vertical levels. The MERRA2 and M2AMIP output are interpolated to a vertical resolution of 240 m before composite.

The time span of MERRA2 for analyzing the TC-radiative interaction matches the CloudSat measurement from 2006 to 2019 (using the 1980-2019 MERRA2 dataset yields similar results). While only one member in M2AMIP that provides the necessary sub-daily data and only over two years (1984–1985 with total 84 TCs; Wing et al. 2019) is examined. The TCs in MERRA2 are tracked by the TempestExtremes tracking algorithm (Ullrich and Zarzycki, 2017). As for M2AMIP, we utilize the TC tracking from Wing et al. (2019), which used the Camargo and Zebiak (2002) tracking algorithm. The composite is conducted on the latitude-longitude grid spacing for both MERRA2 and M2AMIP, while in MERRA2, an additional composite under radius-height composite is conducted under a set of random overpasses mimicking the CloudSat overpasses by randomly create an overpass for each snapshot of TC cases with the same radial bin size for composite and horizontal grid spacing along the overpasses. The sensitivity of the composite from using the snapshot and CloudSat-like overpasses is small. Therefore, the composites from the CloudSat-like overpasses are used for further invectigation. The composites are also categorized by TC intensity (binned by 3 m s^{-1}) of each snapshot and overpass.

**Corresponding author information: Tsung-Yung Lee, Department of Earth, Ocean, and Atmospheric Science, Florida State University, 1011 Academic Way, Tallahassee, FL 32306; Email: tl21q@fsu.edu*

3. THERMODYNAMIC AND CLOUD STRUCTURE

The TC intensity composites of water vapor path (WVP), ice water path (IWP) and liquid water path (LWP) averaged over 200, 500 and 1000 km in radius are shown in Fig. 1. The CSTC composites show the increasing trend of inner-core (200-km average) WVP, IWP and LWP when TC intensity becomes more intense. The increasing trend in the inner-core WVP is also supported by the Advanced Microwave Scanning Radiometer for Earth observing system (AMSR-E) PW product (Moncrieff et al. 2012; Waliser et al. 2012) with a bias around -5 kg m^{-2}. However, the inner-core WVP, IWP and LWP in MERRA2 and GEOS show substantial differences compared to CSTC. The inner-core WVP composites in MERRA2 and GEOS are comparable to each other and significantly larger than that of CSTC, especially for intense TCs. This result is also present in the 500-km average. Though, there's no apparent difference in 1000-km average, expect for weak TCs as GEOS has lower 1000-km average in WVP. The IWP is of an order larger in CSTC compared to both MERRA2 and GEOS regardless of the range for averaging, consistent with the comparison in IWP between CloudSat measurement and MERRA2 over in 60S to 60N in Duncan and Eriksson (2018). The inner-core LWP is much greater in CSTC than that in MERRA2 and GEOS, while the 1000-km average of all datasets show comparable values.

When examining the radius-height structure of the radial anomalies of water vapor mixing ratio (radial anomalies are calculated from the composite mean with respect to the radial mean within 1000-km radius of the composite mean at each height) for the TC intensity bin of 27-30 m s^{-1} as an example, MERRA2 and GEOS both demonstrate that the radial anomalies of water vapor mixing ratio have a substantial positive bias than that in CSTC (Fig. 2). This result from the greater amount of water vapor within 200-km radius and less amount of water vapor beyond 200-km radius below 3-km height (not shown).

As for the ice water mixing ratio (Fig. 3), CSTC depicts a significant greater ice mass than MERRA2 and GEOS. While MERRA2 and GEOS have similar structure for ice water mixing ratio, MERRA2 have a lower bias in upper-tropospheric ice water mixing ratio (~10^{-4} kg kg^{-1}). We will further indicate that this small difference in upper-tropospheric ice water mixing ratio can cause great influence in cloud-LW radiative interaction.

The liquid water mixing ratio is much greater in CSTC, while the structure of liquid water contains several layers of local maximum in MERRA2 and GEOS (Fig. 4). MERRA2 has a low bias beyond 200-km radius and below 5-km height and a positive bias at other regions below 10-km height.

As the radial-height structure of cloud properties exhibit substantial difference between CSTC, MERRA2 and GEOS, the estimation of TC-radiative interaction is expected to vary across these datasets.

4. RADIATIVE FEEDBACKS

The radiative feedback is quantified by utilizing the column-integrated moist static energy (h) variance budget (Wing and Emanuel 2014): $\frac{1}{2}\frac{\partial(\hat{h}'^2)}{\partial t} = \hat{h}' \cdot \mathrm{SEF}' + \hat{h}' \cdot \mathrm{N'_{SW}} + \hat{h}' \cdot \mathrm{N'_{LW}} - \hat{h}'\nabla \cdot \mathrm{N'_{ADV}}$, where h is MSE, $\hat{h}$ indicates the column-integrated MSE, the prime means the anomalies from the radial average within 1000-km radius from the TC center, $\hat{h}'^2$ is the spatial variance of $\hat{h}$, N_{SW} and N_{LW} are the column-net radiative flux convergence for SW and LW, respectively, and $\nabla \cdot \mathrm{N'_{ADV}}$ is the horizontal divergence of the column-integrated lateral fluxes of MSE. Therefore, the longwave (LW) and shortwave (SW) radiative feedbacks are referring $\hat{h}' \cdot \mathrm{N'_{SW}}$ and $\hat{h}' \cdot \mathrm{N'_{LW}}$, respectively. SW feedback is only calculated at daytime. Note that positive radiative feedback indicates the high-energy regimes are warming more or cooling less than the low-energy regimes, leading to greater spatial variance of MSE.

As shown in Fig. 5, the LW feedback in TCs is generally positive for all intensity bins and all radial averages with inner-core LW feedback stronger than the domain-mean LW feedback, consistent with previous studies (e.g. Dirkes et al. 2023). The total-sky LW feedback is strongest in GEOS and moderate in MERRA2, while CSTC shows weakest positive value. The difference between MERRA2 and CSTC comes mainly from the clear-sky effect which is corresponding to the greater inner-core water vapor mixing ratio anomalies in MERRA2 (Fig. 2). With even greater anomalies of the inner-core water vapor mixing (Fig. 2), GEOS experiences a further enhanced clear-sky effect on LW feedback (Fig. 5). It indicates that the positive bias in the inner-core water vapor mixing ratio anomalies originates from the GEOS model, while data assimilation slightly mitigates these anomalies. On the other hand, the cloud effect on LW feedback is greatest in GEOS and comparable in MERRA2 and CSTC. This result might come from the high efficiency of small amount of upper-tropospheric cloud ice to induce the greenhouse effect and reduce the outgoing LW. Since upper-tropospheric cloud ice in MERRA2 and GEOS concentrated within 300-km radius, a comparable effect on generating comparable (or greater) LW anomalies in the TC inner-core might be possible. Further analyses on the outgoing LW radiation and optical depth for LW are needed.

For the total-sky daytime SW feedback (Fig. 6), while CSTC demonstrated negative feedbacks for all TC intensity bins and all radial average, TCs in MERRA2 and GEOS generally experience positive total-sky daytime SW feedback. Comparable cloud effects on daytime SW feedback are shown in CSTC, MERRA2 and GEOS which indicated the low sensitivity of direct column-net absorption of SW radiation from the cloud hydrometeors. Though, the greater water vapor mixing ratio anomalies in MERRA2 and GEOS leads to greater clear-sky daytime SW feedback since the increase in the inner-core water vapor mixing ratio anomalies can effectively increase the absorption of SW radiation. Further analyses on the optical depth for SW are also needed.

5. DISCUSSION AND CONCLUSIONS

In this study, the comparison in thermodynamic and cloud properties and TC-radiative interaction between CSTC, MERRA2 and GEOS is analyzed. Comparing to previous studies, we are the first to link the radius-height structure of thermodynamic and cloud properties to the TC-radiative interaction.

GEOS generates substantially greater LW and daytime SW feedback which is also shown in Wing et al. (2019) where GEOS model is an outlier for the positive radiative feedback among other climate models. This result comes from the excessively greater inner-core water vapor mixing ratio anomalies in GEOS which increases the positive value of clear-sky effect for both LW and daytime SW feedback. In addition, while the IWP is significantly lower in GEOS with respect to CSTC, the upper-tropospheric ice water could efficiently cause greater positive anomalies in column-net LW flux in the TC inner core. Note that the cloud effect on daytime SW feedback is negative and comparable in all datasets, which might result from the reflection of the incoming SW radiation, leading to weaker absorption of SW by water vapor in the TC inner core (Lee and Wing 2024).

The data assimilation processes of MERRA2 lead to slightly weaker inner-core water vapor anomalies, which reduces the positive value of clear-sky effect for both LW and daytime SW feedback with respect to GEOS. However, all of them are still greater than that in CSTC. Meanwhile, the data assimilation processes of MERRA2 lead to comparable cloud effect for both LW and daytime SW feedback with respect to CSTC, while the structure and amount of ice and liquid water are substantially different from CSTC. This result leads to significant difference in the radiative heating structure between CSTC and MERRA2 (not shown) which might generate weaker and top-heavy circulation in MERRA2 and GEOS. As deep in-up-out transverse circulation benefit TC development (Lee and Wing 2024), top-heavy circulation in MERRA2 and GEOS might not effectively spin up the TCs, leading to weaker TC intensity spectrum in MERRA2 and GEOS with respect to the best-track dataset (Wing et al. 2019; Dirkes et al. 2023). Further analyses in the OLR and the optical depths for SW and LW are needed. Moreover, the source of the difference in WVP, IWP and LWP could be the result of using convective parameterization in climate models The radiative scheme could be another source of discrepancy. Both require further investigations.

References

Aarons, Z., S. Camargo, J. Strong, and H. Murakami, 2021: Tropical cyclone characteristics in the MERRA-2 reanalysis and AMIP simulations. Earth and Space Sciences, 8, e2020EA001415, https://doi.org/10.1029/2020EA001415

Austin, R. T., A. J. Heymsfield, and G. L. Stephens, 2009: Retrieval of ice cloud microphysical parameters using the CloudSat millimeter-wave radar and temperature. J. Geophys. Res., 114, D00A23, https://doi.org/10.109/2008JD010049.

Austin, R. T., and N. Wood, 2018: Level 2B radar-only cloud water content (2B-CWC-RO) process description and interface control document, product version P1 R05. NASA JPL CloudSat Project document revision 0, 51 pp.

Camargo, S. J., and S. E. Zebiak, 2002: Improving the detection and tracking of tropical cyclones in atmospheric general circulation models. Weather and Forecasting, 17 (6), 1152-1162, https://doi.org/10.1175/1520-0434(2002)017<1152:ITDATO>2.0.CO;2.

Camargo, S. J. and A. A. Wing, 2016: Tropical cyclones in climate models. WIREs Clim Change, 7: 211-237, https://doi.org/10.1002/wcc.373.

Carstens, J. D., and A. A. Wing, 2020: Tropical cyclogenesis from self-aggregated convection in numerical simulations of rotating radiative-convective equilibrium. Journal of Advances in Modeling Earth Systems, 12, e2019MS002020.

Carstens, J. D., and A. A. Wing, 2022a: A spectrum of convective self-aggregation based on background rotation. Journal of Advances in Modeling Earth Systems, 14, 2021MS002860.

Carstens, J. D., and A. A. Wing, 2022b: Simulating dropsondes to assess moist static energy variability in tropical cyclones. Geophysical Research Letters, 49, e2022GL099101.

Clough, S. A., M. W. Shephard, E. J. Mlawer, J. S. Delamere, M. J. Iacono, K. Cady-Pereira, S. Boukabara, and P. D. Brown, 2005: Atmospheric radiative transfer modeling: A summary of the AER codes. J. Quant. Spectrosc. Radiat. Transfer, 91, 233–244, https://doi.org/10.1016/j.jqsrt.2004.05.058.

Deng, M., G. Mace, Z. Wang, and E. Berry, 2015: CloudSat 2C-ICE product update with a new Ze parameterization in lidar-only region. J. Geophys. Res., 120, 12 198–12 208, https://doi.org/10.1002/2015JD023600.

Deng, M., G. Mace, Z. Wang, and H. Okamato, 2010: Tropical composition, cloud and climate coupling experiment validation for cirrus cloud profiling retrieval using CloudSat radar and CALIPSO lidar. J. Geophys. Res., 115, D00J15, https://doi.org/10.1029/2009JD013104.

Deng, M., G. G. Mace, Z. Wang, and R. P. Lawson, 2013: Evaluation of several A-Train ice cloud retrieval products with in situ measurements collected during the SPARTICUS campaign. J. Appl. Meteor. Climatol., 52, 1014–1030, https://doi.org/10.1175/JAMC-D-12-054.1.

Dirkes, C. A., A. A. Wing, S. J. Camargo, and D. Kim, 2023: Process-Oriented Diagnosis of Tropical Cyclones in Reanalyses Using a Moist Static Energy Variance Budget. J. Climate, 36, 5293–5317, https://doi.org/10.1175/JCLI-D-22-0384.1.

Duncan, D., and P. Eriksson, 2018: An update on global atmospheric ice estimates from satellite observations and reanalyses. Atmos. Chem. Phys., 18, 11 205–11 219, https://doi.org/10.5194/acp-18-11205-2018.

L'Ecuyer, T., N. B. Wood, T. Haladay, G. L. Stephens, and P. W. Stackhouse, Jr, 2008: Impact of clouds on atmospheric heating based on the R04 CloudSat fluxes and heating rates data set. J. Geophys. Res., 113, D00A15. https://doi.org/10.1029/2008JD009951

Gelaro, R., and Coauthors, 2017: The Modern-Era Retrospective analysis for Research and Applications, version 2 (MERRA-2). Journal of Climate, 30 (14), 5419-5454. https://doi.org/10.1175/JCLI-D-16-0758.1

Iacono, M. J., J. S. Delamere, E. J. Mlawer, M. W. Shephard, S. A. Clough, and W. D. Collins, 2008: Radiative forcing by long-lived greenhousegases: calculations with the AER radiative transfer models. J. Geophys. Res., 113, D13 103, https://doi.org/10.1029/2008JD009944.

Jones, E., A. A. Wing, and R. Parfitt, 2021: A global perspective of tropical cyclone precipitation in reanalyses. J. Climate, 34, 8461–8480, https://doi.org/10.1175/JCLI-D-20-0892.1.

Kleist, D., D. Parrish, J. Derber, R. Treadon, W.-S. Wu, and S. Lord, 2009: Introduction of the GSI into the NCEP's global data assimilation system. Wea. Forecasting, 24, 1691-1705. https://doi.org/10.1175/2009WAF2222201.1

Knapp, K. R., H. J. Diamond, J. P. Kossin, M. C. Kruk, and C. J. Schreck, 2018: International Best Track Archive for Climate Stewardship (IBTrACS) project, version 4. Accessed Dec 10, 2021, https://doi.org/10.25921/82ty-9e16.

Knapp, K. R., M. C. Kruk, D. H. Levinson, H. J. Diamond, and C. J. Neumann, 2010: The international best track archive for climate stewardship (IBTrACS): Unifying tropical cyclone data. Bull. Amer. Meteor. Soc., 91 (3), 363–376, https://doi.org/10.1175/2009BAMS2755.1.

Kruk, M. C., K. R. Knapp, and D. H. Levinson, 2010: A technique for combining global tropical cyclone best track data. J. Atmos. Oceanic Technol., 27, 680–692, https://doi.org/10.1175/2009JTECHA1267.1.

Lee, T.-Y. and A. A. Wing: Satellite-Based Estimation of the Role of Cloud-Radiative Interaction in Accelerating Tropical Cyclone Development, J. Atmos. Sci., accepted.

Mlawer, E. J., S. J. Taubman, P. D. Brown, M. J. Iacono, and S. A. Clough, 1997: Radiative transfer for inhomogeneous atmospheres: RRTM, a validated correlated-k model for the longwave. J. Geophys. Res., 102, 16 663–16 682, https://doi.org/10.1029/97JD00237.

Molod, A., L. Takacs, M. Suarez, and J. Bacmeister, 2015: Development of the GEOS-5 atmospheric general circulation model: Evolution from MERRA to MERRA2. Geoscientific Model Development, 8 (5), 1339–1356. https://doi.org/10.5194/gmd-8-1339-2015.

Moncrieff, M., D. Waliser, M. Miller, M. Shapiro, G. Asrar, and J. Caughey, 2012: Multiscale convective organization and the YOTC virtual global field campaign. Bull. Amer. Meteor. Soc., 93, 1171-1187. https://doi.org/10.1175/BAMS-D-11-00233.1

Parker, W. S., 2016: Reanalyses and observations: What's the difference? Bull. Amer. Meteor. Soc., 97, 1565–1572, https://doi.org/10.1175/BAMS-D-14-00226.1.

Rienecker, M., and Coauthors, 2008: The GEOS-5 data assimilation system, documentation of versions 5.0.1, 5.1.0, and 5.2.0. NASA/TM-2008-104606, Vol. 27, 101 pp. Retrieved from https://gmao.gsfc.nasa.gov/pubs/docs/Rienecker369.pdf.

Ruppert, J. H., A. A. Wing, X. Tang, and E. L. Duran, 2020: The critical role of clouds infrared radiation feedback in tropical cyclone development. Proc. Natl. Acad. Sci., 117, 27884–27892, https://doi.org/10.1073/pnas.2013584117.

Tourville, N., G. Stephens, M. DeMaria, and D.Vane, 2015: Remote sensing of tropical cyclones observations from CloudSat and A-Train profilers. Bull. Am. Meteorol. Soc., 96, 609–622, https://doi.org/10.1175/BAMS-D-13-00282.1.

Ullrich, P. A., and C. M. Zarzycki, 2017: TempestExtremes: A framework for scale-insensitive pointwise feature tracking on unstructured grids. Geoscientific Model Development, 10 (3), 1069–1090, https://doi.org/10.5194/gmd-10-1069-2017

Uppala, S. M., and Coauthors, 2005: The ERA-40 re-analysis. Q. J. R. Meteorol. Soc., 131, 2961–3012, https://doi.org/10.1256/qj.04.176.

Waliser, D., and Coauthors, 2012: The "year" of tropical convection (May 2008 to April 2010): Climate variability and weather highlights. Bull. Amer. Meteor. Soc., 93, 1189-1218. https://doi.org/10.1175/2011BAMS3095.1

Wing, A. A. and K. A. Emanuel 2014: Physical mechanisms controlling self-aggregation of convection in idealized numerical modeling simulations, J. Adv. Model. Earth Sys., 6, 59-74, doi:10.1002/2013MS000269.

Wing, A. A., S. J. Camargo, and A. H. Sobel, 2016: Role of radiative–convective feedbacks in spontaneous tropical cyclogenesis in idealized numerical simulations. J. Atmos. Sci., 73, 2633–2642, doi:10.1175/JAS-D-15-0380.1.

Wing, A. A., and Coauthors, 2019: Moist Static Energy Budget Analysis of Tropical Cyclone Intensification in High-Resolution Climate Models. J. Climate, 32, 6071–6095, https://doi.org/10.1175/JCLI-D-18-0599.1.

Wu, W.-S., R. Purser, and D. Parrish, 2002: Three-dimensional variational analysis with spatially inhomogenous covariances. Mon. Wea. Rev., 130 , 2905-2916, https://doi.org/10.1175/15200493(2002)130<2905:TDVAWS>2.0.CO;2.

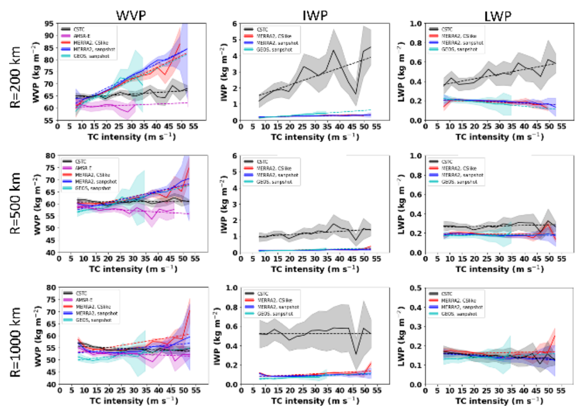

FIGURE 1: The TC intensity composite of water vapor path (WVP; left column), ice water path (IWP; middle column) and liquid water path (LWP; right column) averaged over 200 (top row), 500 (middle row) and 1000 (bottom row) km. Solid lines represent the composite mean, while shaded areas denote the range of the 95% confidence estimated from the student's t test. The dashed lines are the linear regression lines between each variable and TC intensity. The composite based on the CloudSat overpasses is denoted as CSTC in black. The composite based on the CloudSat-like overpasses in MERRA2 snapshots is plotted in red. The composites based on the MERRA2 and M2AMIP (GEOS) snapshots is plotted in blue and cyan, respectively. The magenta lines in the left column are the WVP composite from the Advanced Microwave Scanning Radiometer for Earth observing system (AMSR-E) PW product (Moncrieff et al. 2012; Waliser et al. 2012) for CloudSsat overpasses in TCs during 2009-2011.

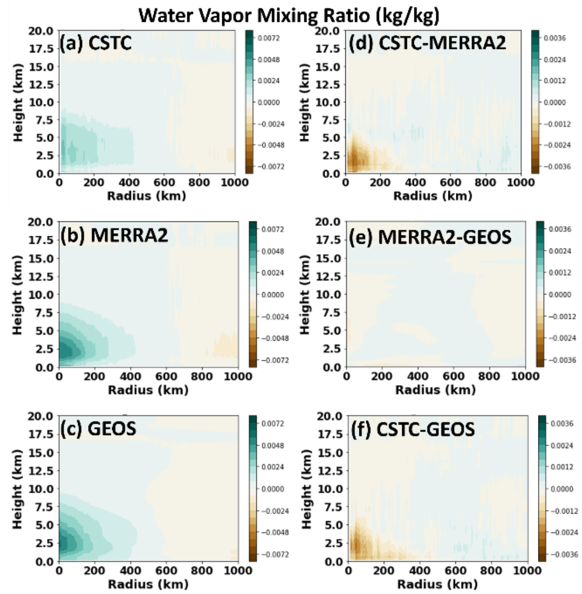

FIGURE 2: The radius-height composite of water vapor mixing ratio (kg kg^{-1}) for (a) CSTC, (b) MERRA2 and (c) GEOS dataset for the TC intensity bin if 27-30 m s^{-1}. The differences between each dataset are shown in the right column as indicated by the text. Note that the scale is different between the left and right columns.

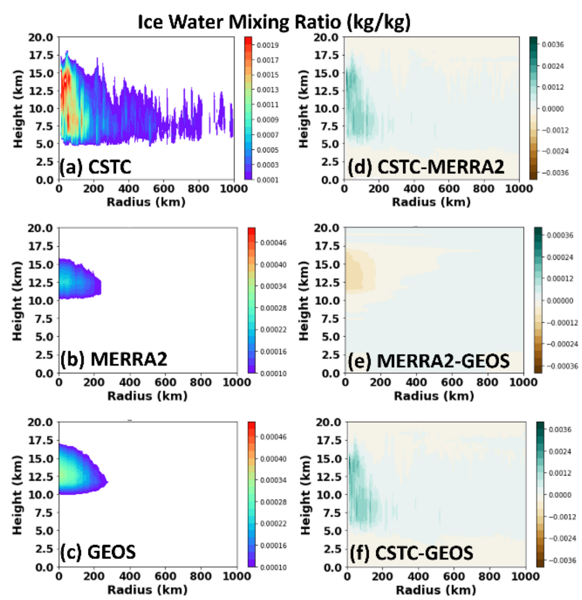

FIGURE 3: The radius-height composite of ice water mixing ratio (kg kg^{-1}) for (a) CSTC, (b) MERRA2 and (c) GEOS dataset for the TC intensity bin if 27-30 m s^{-1}. The differences between each dataset are shown in the right column as indicated by the text. Note that the scale is smaller in an order for (b) and (c) compared to (a) as. Similarly, the scale of (e) is order-smaller than (d) and (f).

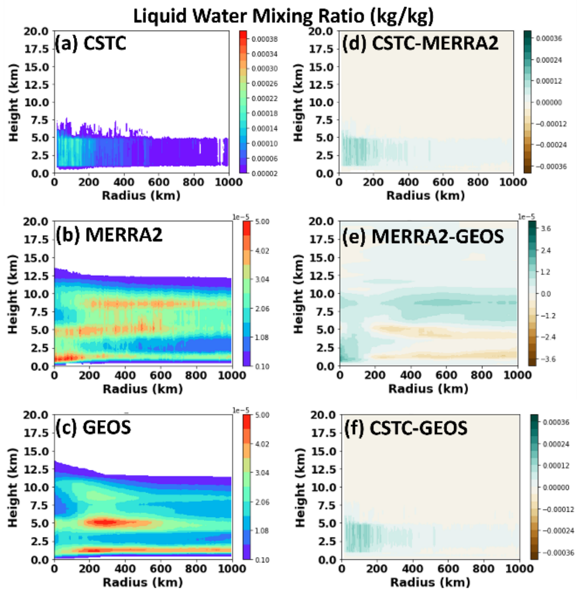

FIGURE 4: As Fig. 3, but for liquid water mixing ratio.

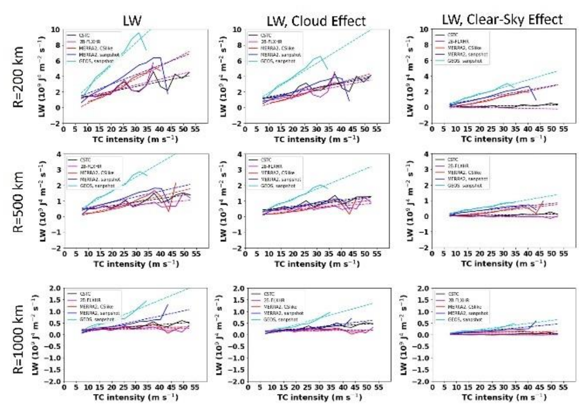

FIGURE 5: The TC intensity composite of the total-sky (left column), cloud (middle column) and clear-sky (LWP; right column) effect on the LW radiative feedback averaged over 200 (top row), 500 (middle row) and 1000 (bottom row) km. The radiative feedbacks are calculated by the radial anomalies of composite mean with respect to the 1000-km radial mean of the composite-mean MSE and column-net radiative fluxes. The line colors are the same as Fig. 1 except that magenta is now showing the radiative feedback calculated from the 2B-FLXHR radiative fluxes (L'Ecuyer et al. 2008) in the CSTC dataset over the CloudSat overpasses.

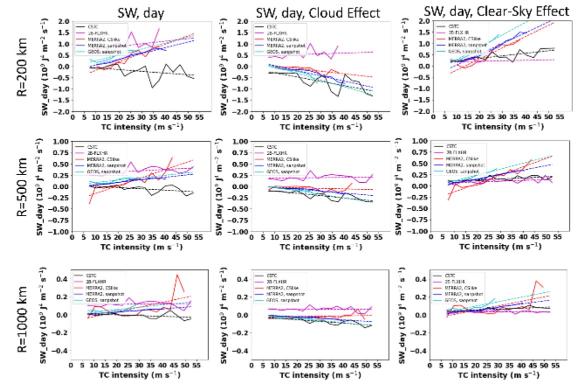

FIGURE 6: As Fig. 5, but for the daytime SW radiative feedbacks.